
END-TO-END INVERSE DESIGNED METASURFACES FOR SNAPSHOT RGB-ACHROMATIC FULL-STOKES POLARIZATION IMAGING

Xingyu Chai

Department of Electronic and Science and Engineering, Southeast University,
2 Sipailou, Xuanwu District, Nanjing, Jiangsu, 210096, China
220241909@seu.edu.cn

Jirong Bao

Department of Electronic and Science and Engineering, Southeast University,
2 Sipailou, Xuanwu District, Nanjing, Jiangsu, 210096, China
213221127@seu.edu.cn

Haining Yang

Department of Electronic and Science and Engineering, Southeast University,
2 Sipailou, Xuanwu District, Nanjing, Jiangsu, 210096, China
h.yang@seu.edu.cn

Mengdi Sun *

Department of Electronic and Science and Engineering, Southeast University,
2 Sipailou, Xuanwu District, Nanjing, Jiangsu, 210096, China
smd@seu.edu.cn

April 17, 2026

ABSTRACT

Snapshot full-Stokes polarimetry across multiple wavelengths remains challenging because conventional architectures rely on multiplexed measurements and bulky optics. We present an end-to-end framework that reconstructs RGB full-Stokes images from a single monochrome sensor measurement. The system combines a differentiable $4f$ optical frontend with a U-Net backend for joint optimization. Notably, a metasurface modeled by the multilayer perceptron (MLP) is employed to encode the full-Stokes polarization information. We implement the design in two stages: first in a hybrid metasurface-refractive $4f$ architecture, and then in a pure meta-optic configuration. On a real-world dataset, the hybrid metasurface-refractive system achieves 30.00 dB peak signal-to-noise ratio (PSNR) and 0.8291 structural similarity index measure (SSIM) for monochromatic imaging in the visible range, and 26.71 dB and 0.7044 for RGB-achromatic imaging. The pure meta-optic system yields 26.94 dB/0.7184 for the monochromatic case and 24.10 dB/0.6015 for the RGB-achromatic case. These results show that end-to-end optical-digital co-design enables compact snapshot full-Stokes polarimetric imaging at a high compression ratio of 12.

Keywords end-to-end optimization · metasurfaces · full-Stokes polarization imaging · snapshot imaging

1 Introduction

Polarization imaging provides information beyond conventional intensity imaging by probing the vector nature of light. In particular, full-Stokes measurements capture both linear and circular polarization components and therefore enable richer characterization of surface roughness [1], depolarization [2], multiple scattering [3–5], and chiral or anisotropic responses [6–9], with applications ranging from scene understanding and remote sensing to imaging in challenging environments [10–12]. However, most full-Stokes imaging systems still rely on spatial or temporal multiplexing using polarizers, wave plates, or division-of-focal-plane architectures. These strategies typically increase system complexity and often sacrifice light throughput, spatial resolution, or snapshot capability, which limits their use in compact and high-speed imaging platforms [13–15].

Metasurfaces offer a promising route to compact polarization-sensitive optics because subwavelength meta-atoms can tailor amplitude, phase, and polarization response within an ultrathin form factor [16, 17]. This capability has motivated a broad range of meta-optic polarization and spectro-polarimetric devices [18, 19]. Yet many existing systems prescribe the optical response a priori and treat reconstruction as a separate downstream problem, or they target only part of the polarization state. For snapshot full-Stokes imaging, especially when spectral information is also encoded, such separately designed systems can lead to a poorly conditioned inverse problem that is sensitive to noise, model mismatch, and spectral-polarimetric crosstalk [14].

In parallel, computational imaging has increasingly shifted from post hoc reconstruction to optical-digital co-design, in which the optical frontend and the reconstruction backend are optimized jointly for a target inference task [20]. Recent work has shown that meta-optics can serve not merely as miniature replacements for conventional optics, but as task-specific physical encoders trained together with the reconstruction algorithm [21–26]. This perspective is particularly compelling for full-Stokes imaging, where the sensor measurement is intrinsically compressive and the reconstruction quality depends as much on the optical encoding as on the computational backend.

Here we present an end-to-end meta-optic framework for snapshot RGB-achromatic full-Stokes polarization imaging. Our system combines a differentiable $4f$ frontend with a trainable metasurface at the Fourier-plane and a U-Net reconstruction backend. To minimize the computational cost and make the pipeline compatible with gradient-based optimization, we use a multilayer perceptron (MLP)-based surrogate model to predict the polarization response of the meta-atoms instead of running expensive numerical solvers. We implement the design in two stages: first in a hybrid metasurface-refractive $4f$ architecture, and then in a pure meta-optic configuration in which the refractive lenses are replaced by metalenses. In the first stage, the metasurface geometry, the focal length, and the neural-network weights are co-optimized. In the second stage, the metalens geometries are additionally optimized with the focal length replaced by free-space distances. On a real-world spectro-polarimetric dataset [27], the hybrid system reaches 30.00 dB PSNR and 0.8291 SSIM in the monochromatic case and 26.71 dB and 0.7044 across three RGB wavelengths; the pure meta-optic system retains strong performance, achieving 26.94 dB and 0.7184 for monochromatic imaging and 24.10 dB and 0.6015 for RGB imaging at a relatively high compression ratio of 12. These results show that end-to-end co-design opens a new avenue for compact, snapshot, high-dimensional polarimetric imaging in both hybrid and pure meta-optic systems.

2 Method

Our framework combines a differentiable optical encoder with a neural decoder for snapshot full-Stokes polarization imaging. The optical frontend is based on a $4f$ system with a trainable polarization-sensitive metasurface placed at the Fourier plane, and the computational backend is a U-Net that reconstructs the full-Stokes image cube from a single sensor measurement. To enable efficient end-to-end optimization, both the Fourier-plane metasurface and the metalenses are modeled through an MLP-based surrogate trained on full-wave electromagnetic simulations. In Section 2.1, we detail the design process of the MLP-based surrogate model for the metasurface and the metalenses, as shown in Fig. 1. In Sections 2.2-2.4, we introduce the inverse design framework for full-Stokes polarization imaging, detailing its optical frontend, computational backend and the end-to-end optimization pipeline, as shown in Fig. 4. Notably, the optimization is performed in two stages, as shown in Table 1. In the first stage, a hybrid metasurface–refractive $4f$ system is optimized by jointly updating the metasurface geometry, the focal length, and the neural-network weights. In the second stage, the refractive lenses are replaced by two metalenses for further miniaturization and higher manufacturability, and the meta-optic $4f$ system is re-optimized by jointly updating the metasurface geometry, the metalens geometries, the free-space distances, and the neural-network weights.

Table 1: The optical differentiable configuration corresponding to two stages.

Stage	Optical configuration
Stage 1 (metasurface-refractive $4f$ system)	metasurface geometry, focal length, neural-network weights
Stage 2 (meta-optic $4f$ system)	metalens geometries, metasurface geometry, free-space distances, neural-network weights

2.1 MLP-based surrogate model

The MLP-based surrogate model characterizes the responses of the subwavelength unitcells (meta-atoms) of the metasurface corresponding in the RGB-achromatic case [28, 29]. As shown in Fig. 1a, each meta-atom consists of a TiO_2 rectangular nanopillar on a SiO_2 substrate. The refractive indices of TiO_2 and SiO_2 are taken as 2.55 and 1.45, respectively [30]. The nanopillar height is fixed at $0.8 \mu\text{m}$ for ease of fabrication, whereas the in-plane geometrical parameters, namely the length a , width b , and rotation angle θ , are treated as degrees of freedom. The parameters a and b are varied within the range of $0.05\text{--}0.4 \mu\text{m}$, and θ is swept from 0° to 90° . The unit-cell period is fixed at $0.4 \mu\text{m}$ to suppress higher-order diffraction.

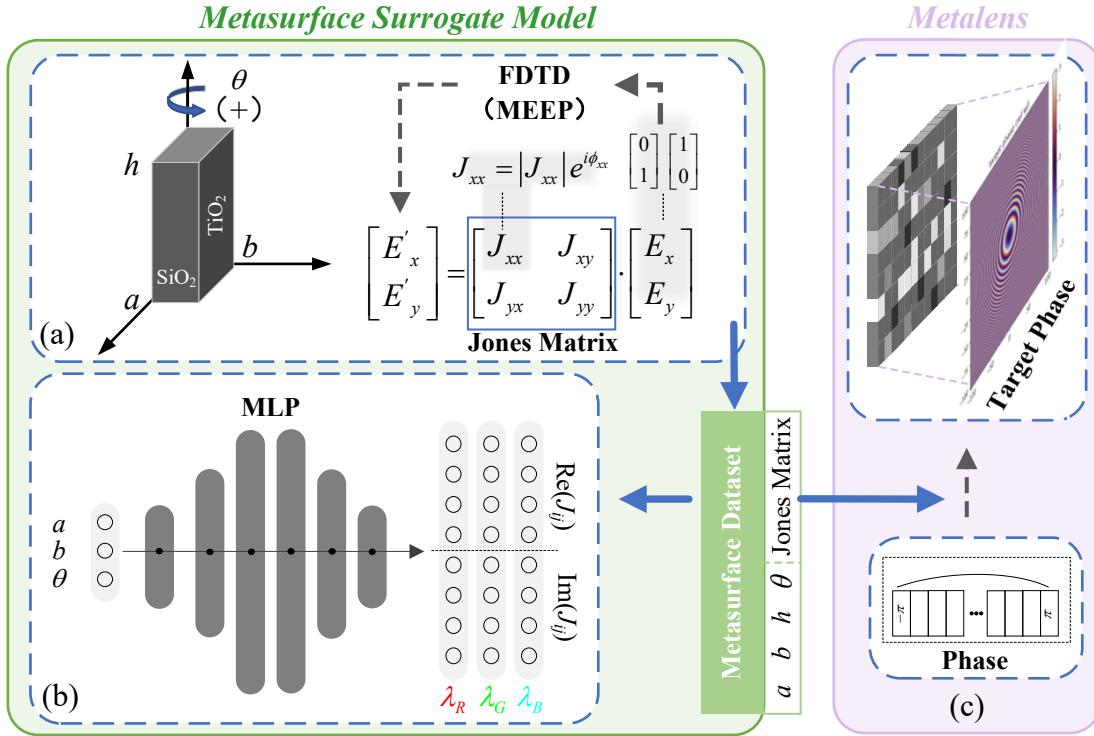


Figure 1: The design process of the MLP-based surrogate model for the metasurface and the metalenses.

For each meta-atom, the local polarization response is described by a 2×2 complex Jones matrix under a complete polarization basis [31]:

$$J(a, b, \theta) = R(-\theta) \begin{bmatrix} e^{i\phi_x(a,b)} & 0 \\ 0 & e^{i\phi_y(a,b)} \end{bmatrix} R(\theta) \quad (1)$$

where the matrix elements encode the amplitude and phase response for orthogonal polarization components. ϕ_x and ϕ_y represent the phase shifts introduced along the nanopillar's principal axes, which are sensitive to a and b .

To generate the surrogate-model dataset, we perform full-wave electromagnetic simulations using the finite-difference time-domain (FDTD) solver in MEEP under the locally periodic approximation (LPA) [32, 33]. LPA is widely used in the design of conventional metasurfaces comprised of nanopillars or nanofins, in which non-local coupling between adjacent meta-atoms is negligible [34–37]. Two orthogonal linearly polarized incident fields, $[1, 0]^T$ and $[0, 1]^T$, are

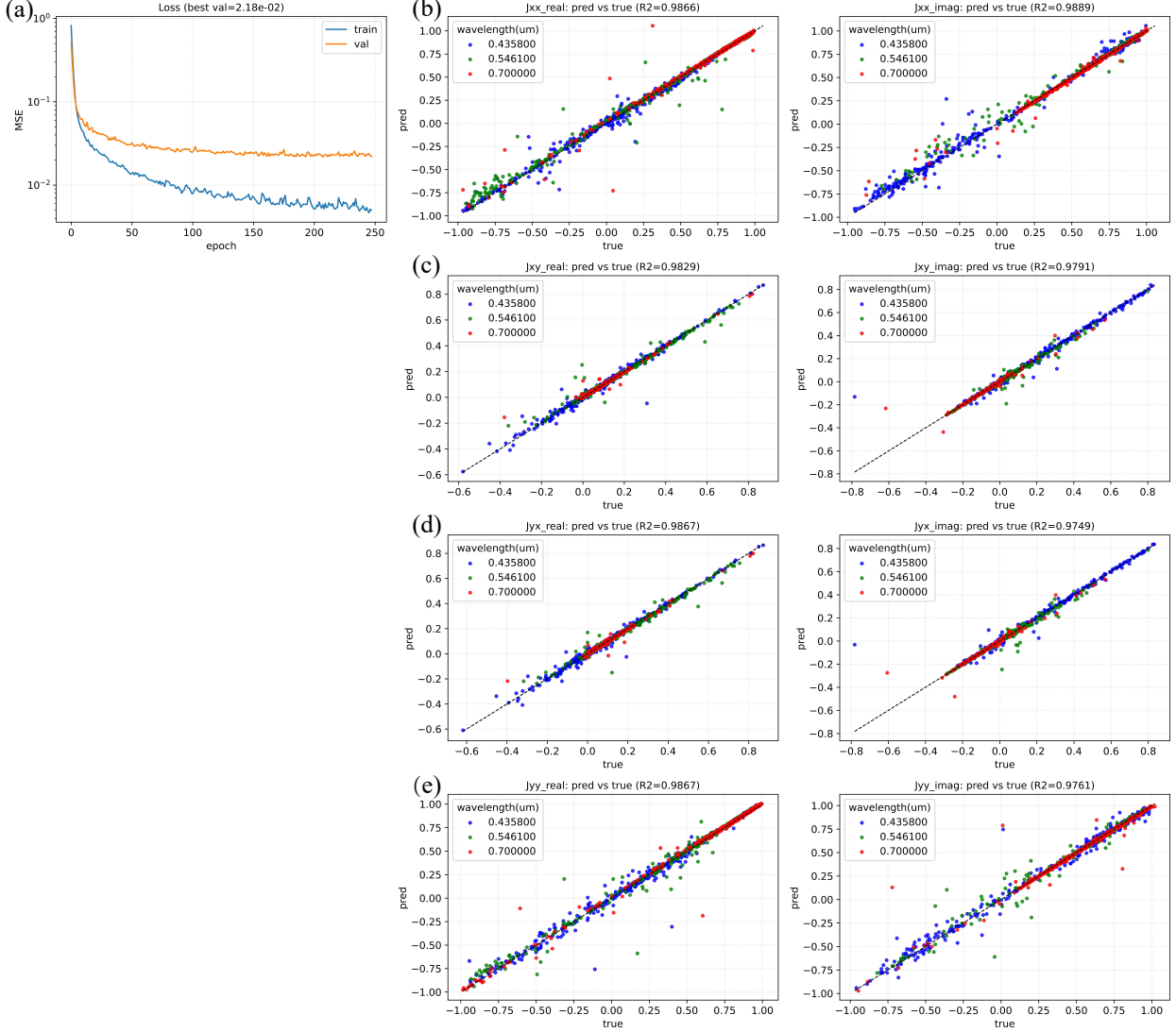


Figure 2: Performance of the MLP-based surrogate model based on the meta-atoms of the metasurface at RGB-achromatic case. (a) Training and validation loss over training epochs. (b-e) Scatter plots of predicted vs. true values (real and imaginary components of the Jones matrix).

used to extract the complex Jones matrices at the RGB-achromatic case. The resulting dataset establishes the mapping between meta-atom geometry and polarization response.

The MLP-based surrogate model is then trained to approximate this mapping, as illustrated in Fig. 1b. The input to the MLP is the set of geometrical parameters $\{a, b, \theta\}$, and the output is the real and imaginary parts of the Jones-matrix elements at the target wavelengths. Once trained, the surrogate model replaces repeated full-wave simulations during system-level optimization and enables efficient backpropagation through the optical frontend. The training loss is defined as the mean squared error (MSE) between the predicted and simulated Jones-matrix elements. The network is trained via custom gradient descent with a learning rate of 10^{-3} and an early stop mechanism, using a training/validation/testing data split of 8:1:1.

The predictive accuracy of the surrogate model is summarized in Fig. 2. As shown in Fig. 2a, the training loss decreases below 10^{-2} , while the validation loss remains below 10^{-1} by the end of training. The regression plots in Fig. 2b-e further confirm strong agreement between simulated and predicted Jones-matrix elements, with the R^2 values around 0.98 across the real and imaginary parts of J_{xx} , J_{xy} , J_{yx} , and J_{yy} at the RGB wavelengths.

In the second stage, we design the metalenses to replace the refractive lenses in a metasurface-refractive $4f$ system for further system miniaturization [16, 38–41]. It should be noted that in the aforementioned metasurface design, $J_{ij} = |J_{ij}| \cdot e^{i\phi_{ij}}$ ($i, j \in \{x, y\}$) describes the linear transformation of the input j polarized component into the output i -polarized component, where ϕ_{ij} represents the imparted geometrical phase [42] for each polarization component combination. Therefore, the geometrical parameters of the metalens can be searched in the same dataset as the metasurface.

We first define the target phase profile of a lens from the optical-path-difference expression:

$$\phi_{\text{lens}}(x, y, \lambda) = -\frac{2\pi}{\lambda} \left(\sqrt{x^2 + y^2 + f^2} - f \right) \quad (2)$$

where f is the design focal length and (x, y) denotes the position on the lens aperture. As shown in Fig. 1c, the target phase profile is discretized into 256 levels over $[-\pi, \pi]$. For each phase level, a candidate meta-atom is selected from the simulated dataset so that the co-polarized phase response matches the target phase as closely as possible while maintaining high transmission and low polarization crosstalk. The metalens design objective therefore combines phase error, transmission penalty, and crosstalk penalty into a weighted scalar loss. This procedure is performed at 435.8 nm to initialize the metalens. For simplicity, instead of re-designing the metalenses for the RGB setting, we directly reuse this 435.8 nm design as the initial structure. Due to the robust convergence of our differentiable end-to-end pipeline, this initial structure can be seamlessly optimized to accommodate RGB performance.

The resulting monochromatic metalens performance is shown in Fig. 3a. The fitted phase profile agrees well with the target phase, yielding $R^2 = 0.998$ and a phase MSE of 0.005128. Fig. 3b further verifies that two such metalenses can form a $4f$ system, which provides a suitable initialization for the end-to-end optimization in the second stage.

2.2 Differentiable Optical Frontend

In the first stage, we consider a polarization-resolved $4f$ system composed of two identical refractive lenses and a trainable metasurface located at the Fourier plane, as shown in Fig. 4. The distances from the objective plane to the first lens z_1 and from the second lens to the sensor plane z_2 are both equal to the focal length f . For each wavelength λ_k , the scene is represented by a spatially varying Jones field $\mathbf{E}_{\text{in}}(\lambda_k)$, derived from the target full-Stokes images. The field propagates through the first lens, the Fourier-plane metasurface, and the second lens before reaching the sensor.

The entire forward pipeline can be formulated as below, and it holds true for all the RGB wavelengths:

$$E_{\text{mask}} = J_{\text{mask}} A_{z1} (\phi_{\text{lens}} A_{z1} (E_{\text{in}})) \quad (3)$$

$$I_{\text{sensor}} = |A_{z2} (\phi_{\text{lens}} A_{z2} (E_{\text{mask}}))|^2 \quad (4)$$

where J_{mask} represents the Jones matrix of the metasurface, ϕ_{lens} is the phase of two identical lenses. E_{mask} is the output fields of the metasurface. To maintain differentiability for end-to-end optimization, we used the angular spectrum propagation method to model the free space propagation of light, where A_{z1} and A_{z2} represent the angular spectrum propagation operators corresponding to the distance z_1 and z_2 . The sensor measures only the scalar intensity I_{sensor} , which compresses the polarization and spectral information into a single channel.

In the second stage, the metalenses designed in Section 2.1, which are described by Jones matrices J_{ml1} and J_{ml2} , are employed to replace the lenses for system miniaturization and improved manufacturability. In the RGB case, a 256×256 sensor measurement is used to reconstruct a $256 \times 256 \times 4 \times 3$ full-Stokes data cube, corresponding to a compression ratio of 12. This makes the reconstruction strongly underdetermined and motivates joint optimization of both the optical frontend and the digital backend.

2.3 Backend

The polarization state of the incident field is represented by the full-Stokes parameters S_0, S_1, S_2 , and S_3 . Recovering these quantities from a single scalar sensor image constitutes a highly underdetermined problem, particularly in the RGB-achromatic case. To address this challenge, we employ a U-Net as the computational backend, as shown in Fig. 5. The architecture of U-Net utilizes a symmetric, hierarchical encoder-decoder structure with skip-connections to fuse multi-scale spatial features, which is crucial for maintaining the fidelity of complex polarization edges and textures that are often blurred in standard auto-encoders. The encoder path progressively processes the input through a series of double convolution blocks with 3×3 convolutional layers, batch normalization, ReLU activation, and dropout regularization with a rate of 0.1, reaching a bottleneck with 512 channels to extract compact abstract representations of the encoded Stokes information. Symmetrically, the decoder path reconstructs the spatial resolution via bilinear interpolation while incorporating the encoder’s high-frequency details through skip-connections. A 1×1 convolutional

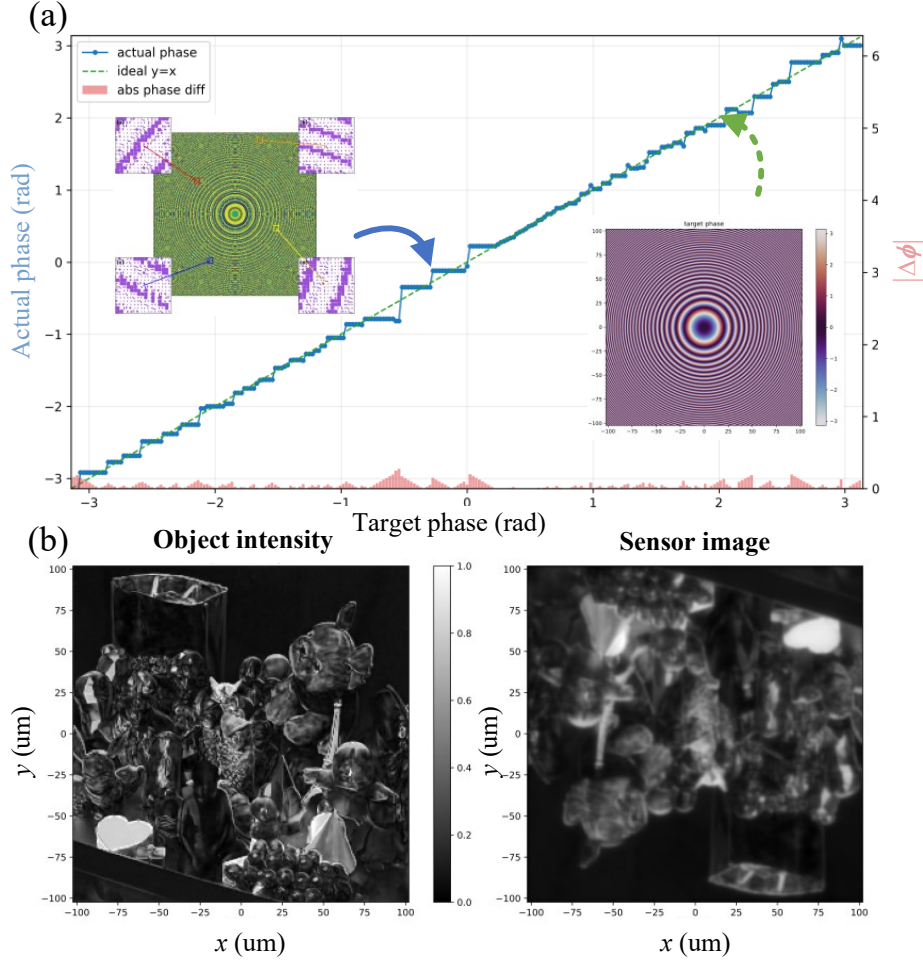


Figure 3: The metalens performance in the monochromatic case at $0.4358 \mu\text{m}$. (a) The error and phase distribution of the actual phase and the target one. (b) The example of the real-world image propagates through meta-optic $4f$ system.

layer is employed at the output to project the decoded features to the target channel dimension, which can be dynamically adjusted based on the number of wavelengths. Additionally, a global residual learning strategy is adopted where the network predicts the deviation from a baseline constructed from the input intensity, facilitating faster convergence during optimization. For each wavelength, the network directly predicts the S_1 , S_2 and S_3 components, while the total intensity S_0 is calculated through a physical consistency constraint for complete polarization based on the vector norm:

$$S_0 = \sqrt{S_1^2 + S_2^2 + S_3^2} \quad (5)$$

U-Net exhibits strong translation invariance via its convolutional architecture, aligning well with the approximately linear shift-invariant (LSI) propagation model of the imaging system [43]. This makes it possible to naturally learn the spatial mapping from sensor intensity measurements to full-Stokes polarization parameters, efficiently overcoming the limitations of handcrafted priors in traditional regularization methods. Moreover, U-Net supports end-to-end optimization with relatively higher computational efficiency than iterative optimization-based methods.

To enforce physical consistency, the loss function includes both pixel-level reconstruction terms and a polarization-structure constraint, as described below. The U-Net is trained jointly with the optical frontend using adaptive gradient descent (Adam) optimizer, a batch size of 4, and an early stop mechanism. The dataset is split into training/validation/testing sets with a ratio of 8.5:1:0.5. The checkpoint with the lowest validation loss is selected for testing.

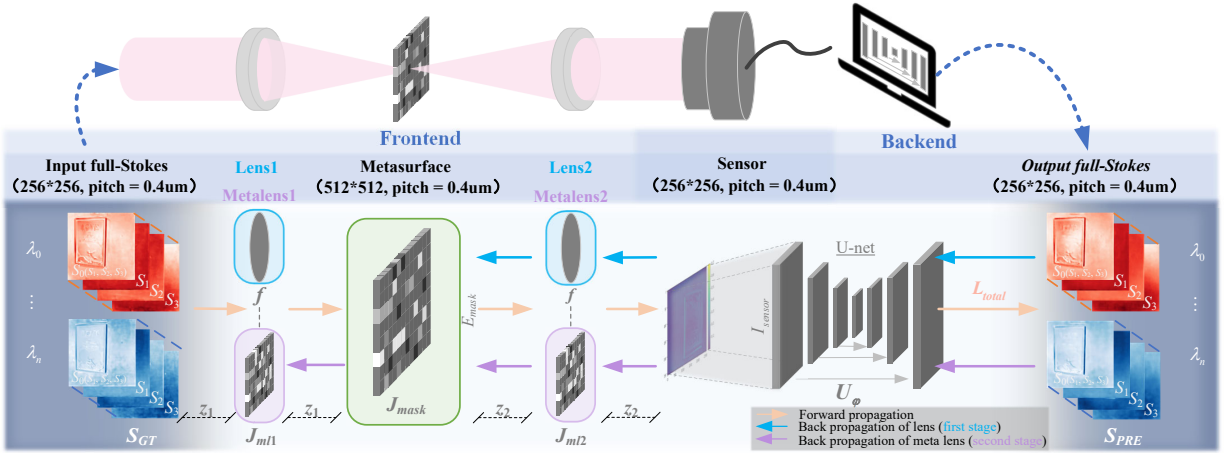


Figure 4: The architecture of the proposed full-Stokes polarization imaging system

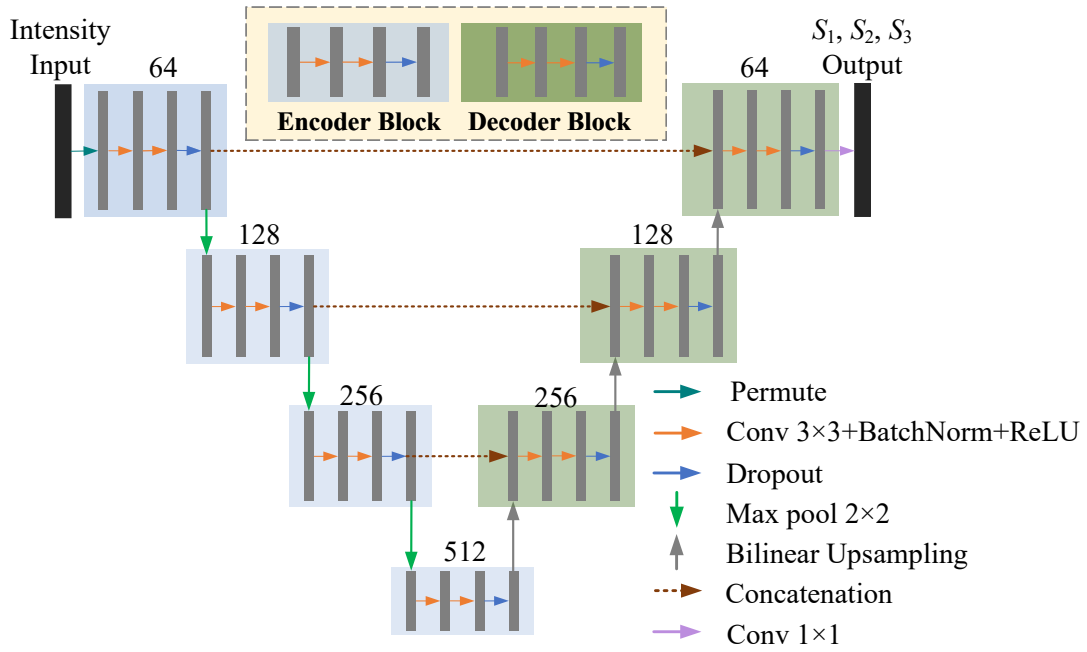


Figure 5: Schematic overview of the U-Net used in the backend. The values above the block represent the number of feature maps produced at each stage.

2.4 End-to-end collaboration

The system is optimized end-to-end based on a multi-objective loss function L_{total} that integrates the image reconstruction fidelity with hardware-level physical constraints. The collaborative refinement ensures high PSNR and SSIM performance even at a significant compression ratio. The total loss L_{total} is defined as:

$$L_{\text{total}} = w_{\text{rec}}L_{\text{rec}} + w_{\text{ssim}}L_{\text{ssim}} + w_{\text{smooth}}L_{\text{smooth}} \quad (6)$$

where L_{rec} combines pixel-level L_1 and L_2 errors with a Sobel gradient loss to maintain high numerical accuracy and edge sharpness, L_{ssim} constrains the structural integrity of the reconstructed Stokes fields and L_{smooth} applies total variation (TV) regularization to the geometrical parameters to ensure spatial smoothness for fabrication and local periodic approximation. The loss weights w_{rec} , w_{ssim} , w_{smooth} are set to 10, 3, 0.01.

In the first stage (the blue arrows in Fig. 4), the trainable variables are the metasurface geometry, the focal length, and the neural-network weights. In the second stage (the purple arrows in Fig. 4), the trainable variables are the metasurface geometry, the two metalens geometries, the free-space distances, and the neural-network weights.

Gradients from L_{total} back propagate through the entire differentiable pipeline, following a chain rule framework for all tunable variables. The core gradient flow for the metasurface geometric parameters is $\{a, b, \theta\}$ expressed as:

$$\frac{\partial L_{\text{total}}}{\partial \{a, b, \theta\}} = \frac{\partial L_{\text{total}}}{\partial U_{\varphi}} \cdot \frac{\partial U_{\varphi}}{\partial I_{\text{sensor}}} \cdot \frac{\partial I_{\text{sensor}}}{\partial E_{\text{mask}}} \cdot \frac{\partial E_{\text{mask}}}{\partial J_{\text{mask}}} \cdot \frac{\partial J_{\text{mask}}}{\partial \{a, b, \theta\}} \quad (7)$$

This multi-scale gradient propagation ensures that every physical and digital parameter is updated in a direction that minimizes the global objective function L_{total} .

This formulation allows the optical encoder and the neural decoder to be refined jointly toward the same objective. Rather than optimizing the optics for a predefined polarization response and training the network afterward, the proposed framework learns an optical encoding strategy that directly matches the reconstruction task and the statistics of the dataset.

3 Results and discussion

We evaluate the proposed framework on the real-world spectro-polarimetric dataset [27], which contains 2022 samples and exhibits substantially richer spatial, spectral, and polarization statistics than the synthetic datasets commonly used in prior works. The dataset is divided into the train sets, validation sets and test sets. The optical setups in two stages are considered across Section 3.1 and 3.2: a hybrid metasurface-refractive $4f$ system in the first stage and a pure meta-optic $4f$ system in the second stage where the refractive lenses are replaced by metalenses. For each setup, to rigorously evaluate the reconstruction capability of the proposed framework, we study both monochromatic and RGB reconstruction and compare three metasurface mask settings: a jointly optimized trained mask with uniform geometric parameters, a fixed random mask with random geometric parameters, and a no-mask baseline without the metasurface, where only the U-Net in the backend is optimized for the latter two cases. Meanwhile, the framework is trained on an NVIDIA GeForce RTX 5090.

3.1 Real-world dataset testing with lenses in the first stage

In the first stage, where a $4f$ system with conventional refractive lenses is employed, metasurface is initialized to a uniform structure as a trained mask and then jointly optimized with the focal length f and neural-network weights φ .

3.1.1 Monochromatic reconstruction

The training is based on the early stop mechanism. The corresponding training curves for the monochromatic case are shown in Fig. 6. The trained-mask configuration converges faster (2.95 hrs) and to a substantially lower validation loss (≈ 0.4) than either the random-mask or no-mask baselines (≈ 1.0), indicating that joint optical-digital optimization improves the conditioning of the inverse problem. In other words, the optimized metasurface produces sensor measurements that are more informative for downstream Stokes recovery than either a random encoding or no encoding at all.

The quantitative comparison results under different masks are summarized in Table 2. The trained-mask configuration achieves an average PSNR of 30.00 dB and an average SSIM of 0.8291, compared with 24.85 dB and 0.6159 for the random-mask baseline and 25.45 dB and 0.6455 for the no-mask baseline. This corresponds to a PSNR gain of 5.15 dB over the random-mask case and 4.55 dB over the no-mask case, together with substantial SSIM improvements. The

MSE is reduced from 1.40×10^{-3} and 1.34×10^{-3} in the two baselines to 4.34×10^{-4} in the trained-mask setting, representing roughly a threefold error reduction. Given the fast transmission speed of physical front-end, we only evaluate the inference speed in the backend. The inference speed remains essentially unchanged at approximately 152 imgs/s, which indicates that the performance gain arises from improved optical encoding rather than additional computational cost in the decoder.

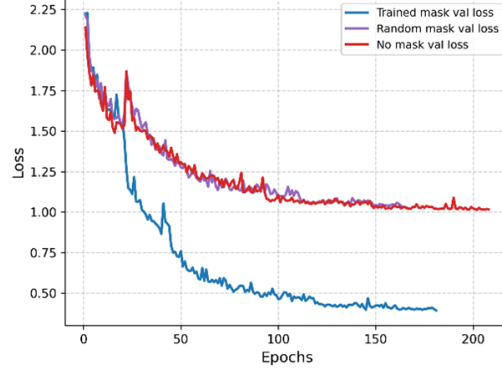


Figure 6: Loss function under different masks over training epochs in the monochromatic case for the first stage.

Table 2: Quantitative comparison of PSNR, SSIM and FPS under different masks in the monochromatic case for the first stage.

Methods	Trained mask	Random mask	no mask
PSNR (dB)	30.00	24.85	25.45
SSIM	0.8291	0.6159	0.6455
MSE	4.34×10^{-4}	1.40×10^{-3}	1.34×10^{-3}
FPS (imgs/s)	151.58	152.06	151.85

3.1.2 RGB-achromatic reconstruction

The RGB reconstruction task is significantly more challenging because the sensor must encode the four Stokes parameters at three wavelengths into a single intensity image with a high compression ratio of 12. Despite this stronger compression, the training remains stable for the trained-mask system, as shown in Fig. 8. The trained mask learns a wavelength- and polarization-dependent measurement operator that allows the U-Net to disentangle the multiplexed information more effectively than in the random-mask and no-mask baselines. The training time of the trained mask is 7.99 hrs.

Table 3 summarizes the quantitative comparisons for the RGB-achromatic cases. The trained-mask configuration achieves an average PSNR of 26.71 dB and an average SSIM of 0.7044, compared with 23.11 dB and 0.5478 for the random-mask baseline and 23.60 dB and 0.5803 for the no-mask baseline. Relative to the random-mask case, the jointly optimized system improves PSNR by 3.60 dB and SSIM by 0.1566. Relative to the no-mask baseline, the gains are 3.11 dB and 0.1241, respectively. Compared to the monochromatic value, although the MSE increases to 8.24×10^{-4} , it remains much lower than those of the baselines, which are on the order of 10^{-3} . The inference speed remains high, with the trained-mask configuration reaching 148.54 imgs/s.

The visual results in Fig. 9 show that the proposed system maintains good reconstruction fidelity across different wavelength channels and Stokes components despite the high compression ratio of 12. Compared with the baselines, the trained-mask system better preserves both spectral consistency and polarization-dependent contrast. This result is important because it shows that the benefit of end-to-end optical design is not limited to the monochromatic case but extends to high-dimensional RGB full-Stokes recovery.

3.2 Real-world dataset testing with metalenses in the second stage

In the second stage, the two refractive lenses are replaced by metalenses, yielding a pure meta-optic $4f$ system. At this point, the trainable focal-length parameter is replaced by the free-space distances z_1 and z_2 . The same three mask settings are used for comparison.

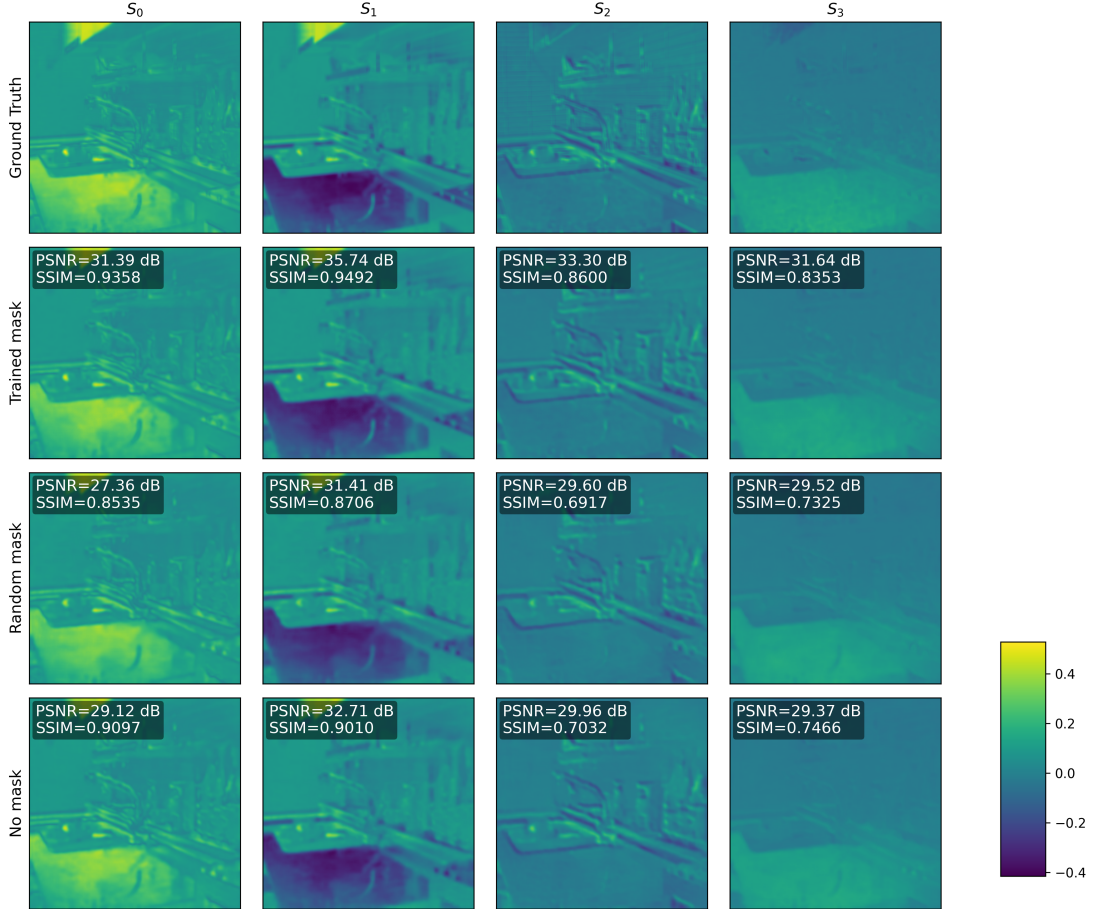


Figure 7: Examples of full-Stokes images reconstructed under different masks in the monochromatic case for the first stage.

Table 3: Quantitative comparison of PSNR, SSIM and FPS under different masks in the RGB-achromatic case for the first stage.

Methods	Trained mask	Random mask	no mask
PSNR (dB)	26.71	23.11	23.60
SSIM	0.7044	0.5478	0.5803
MSE	8.24×10^{-4}	2.03×10^{-3}	1.83×10^{-3}
FPS (imgs/s)	148.54	142.15	143.77

3.2.1 Monochromatic reconstruction

The monochromatic training dynamics are shown in Fig. 10. The trained-mask configuration again converges to a lower validation loss (≈ 0.5) than the random-mask (≈ 1.9) and no-mask (≈ 1.7) baselines, within the training time of 11.08 hrs, although the final loss is higher than that of the metasurface-refractive first stage. This behavior is consistent with the increased difficulty of the pure meta-optic system, where residual phase mismatch, aperture discretization, and optical nonidealities make the forward operator harder to invert.

The quantitative performance is listed in Table 4. The trained-mask configuration achieves an average PSNR of 26.94 dB and an average SSIM of 0.7184, compared with 18.74 dB and 0.3309 for the random-mask baseline and 20.51 dB and 0.4346 for the no-mask baseline. Thus, even in the pure meta-optic system, end-to-end optimization improves PSNR by 8.20 dB over the random-mask case and by 6.43 dB over the no-mask case. The corresponding MSE of the

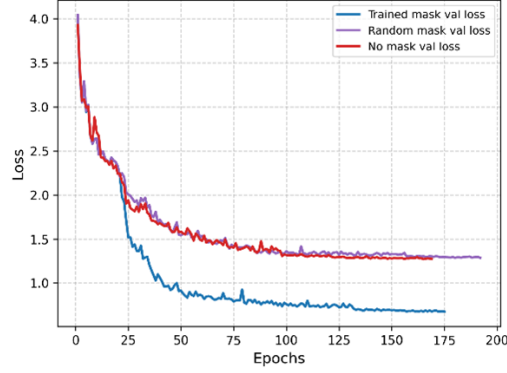


Figure 8: Loss function under different masks over training epochs in the RGB-achromatic case for the first stage.

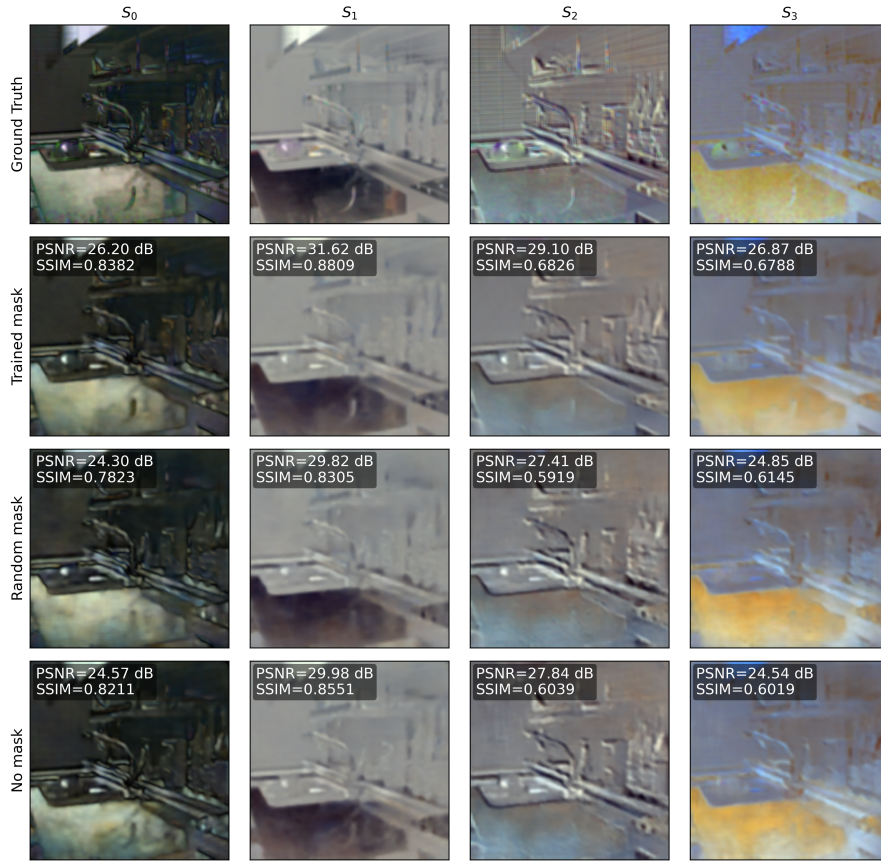


Figure 9: Examples of full-Stokes images reconstructed under different masks in the RGB-achromatic case for the first stage.

trained-mask system is 7.58×10^{-4} , which is smaller than those of the baselines. The inference speed remains high, between 144 and 151 imgs/s.

Visual results in Fig. 11 demonstrate that the trained mask preserves image textures and Stokes-parameter contrast, whereas the random-mask and no-mask cases display strong concentric-ring artifacts. These artifacts are primarily caused by phase discretization and the resulting parasitic diffraction of the metalenses and metasurface. Without an optimized phase profile, these discrete phase errors manifest as the geometric signature of the circular aperture, leading

to an encoding collapse. The reconstruction backend fails to distinguish true object features from this systematic diffraction noise.

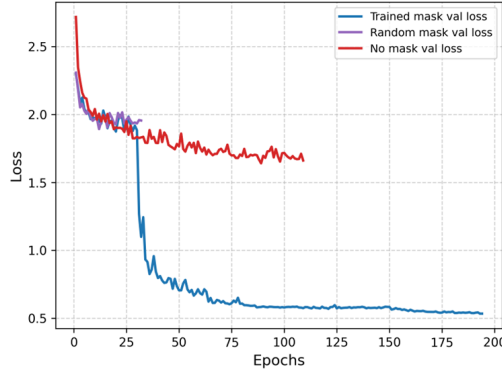


Figure 10: Quantitative comparison of PSNR, SSIM and FPS under different masks in the monochromatic case for the second stage.

Table 4: Quantitative comparison of PSNR, SSIM and FPS under different masks in the monochromatic case for the second stage.

Methods	Trained mask	Random mask	no mask
PSNR (dB)	26.94	18.74	20.51
SSIM	0.7184	0.3309	0.4346
MSE	7.58×10^{-4}	5.03×10^{-3}	3.21×10^{-3}
FPS (imgs/s)	150.58	146.09	144.70

3.2.2 RGB-achromatic reconstruction

The RGB-achromatic training results are shown in Fig. 12. Although in the monochromatic case, the trained-mask configuration achieves a substantially lower validation loss than the baselines, the gap between the trained-mask and baseline curves is even larger here because the RGB task is more severely underdetermined. The validation loss for the trained mask drops sharply around epoch 30 and keeps decreasing steadily to approximately 0.9. The training time within the trained mask is 11.69 hrs.

The trained-mask meta-optic system reaches an average PSNR of 24.10 dB and an average SSIM of 0.6015 at the RGB wavelengths (Table 5), compared with 18.83 dB and 0.3335 for the random-mask baseline and 19.26 dB and 0.3521 for the no-mask baseline. This corresponds to PSNR gains of 5.27 dB and 4.84 dB, respectively, together with marked SSIM improvements. The MSE of the trained-mask system is 1.55×10^{-3} , still significantly smaller than those of the baselines. The inference speed remains close to 150 imgs/s, demonstrating that the pure meta-optic configuration does not compromise the real-time capability of the neural decoder.

As shown in Fig. 13, the trained-mask system reconstructs RGB full-Stokes information with clearly better spatial detail and fewer artifacts than the baselines. The random-mask and no-mask systems exhibit even stronger concentric artifacts than in the monochromatic case, indicating that the metalens-only measurement operator is particularly inadequate for multiplexing both polarization and wavelength information unless the Fourier-plane metasurface is jointly optimized to compensate for chromatic dispersion and phase discretization. Although the RGB meta-optic performance is lower than that of the refractive-lens first stage, the results demonstrate that a pure meta-optic architecture can still support high-dimensional full-Stokes reconstruction by jointly optimizing the optical encoder and the digital decoder.

3.3 Full-Stokes reconstruction performance comparison

To place the results in context, Table 6 compares the proposed framework with representative full-Stokes reconstruction systems reported in the literature. Direct numerical comparison should be interpreted with caution because the reported methods differ in wavelength range, compression setting, dataset type, optical architecture, and evaluation protocol. In particular, many prior works are evaluated on synthetic datasets [4, 21, 22, 44], whereas our results are obtained on a real-world spectro-polarimetric dataset with more complex scene statistics.

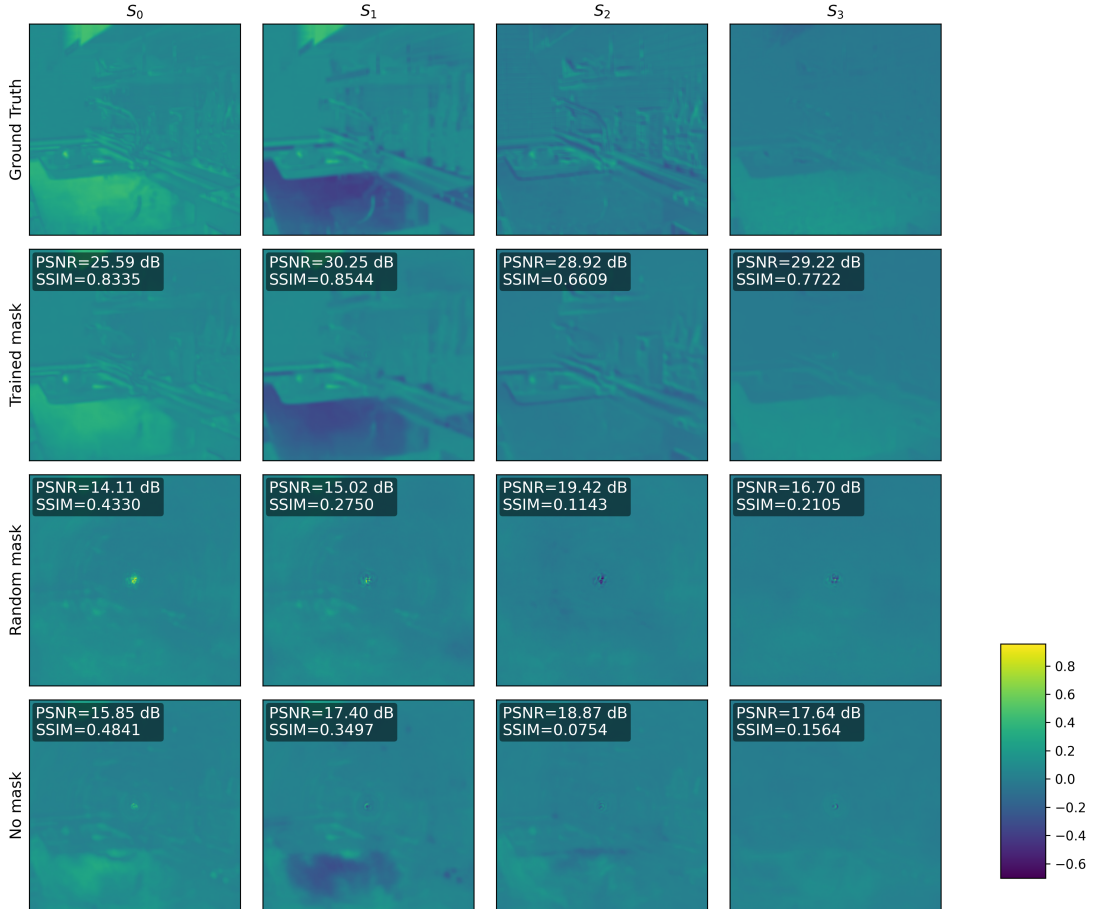


Figure 11: Examples of full-Stokes images reconstructed under different masks in the monochromatic case for the second stage.

Table 5: Quantitative comparison of PSNR, SSIM and FPS under different masks in the RGB-achromatic case for the second stage.

Methods	Trained mask	Random mask	no mask
PSNR (dB)	24.10	18.83	19.26
SSIM	0.6015	0.3335	0.3521
MSE	1.55×10^{-3}	5.47×10^{-3}	4.67×10^{-3}
FPS (imgs/s)	149.50	148.81	143.19

Within this context, the proposed framework remains competitive while operating under aggressive compression. In the lens-based system, the monochromatic configuration achieves 30.00 dB PSNR and 0.8291 SSIM at a compression ratio of 4, while the RGB configuration achieves 26.71 dB and 0.7044 at a compression ratio of 12. In the pure meta-optic $4f$ system, the corresponding values are 26.94 dB and 0.7184 for the monochromatic case and 24.10 dB and 0.6015 for the RGB case. These results show that the proposed end-to-end inverse designed framework can maintain high reconstruction fidelity even when both spectral and polarization information are significantly compressed into a single measurement.

More importantly, the comparison across Tables 2–5 shows that the main advantage of the framework does not arise merely from using a neural decoder, but from jointly optimizing the optical encoder and the reconstruction network. Across both stages and both wavelength settings, the trained-mask configuration consistently outperforms the random-mask and no-mask baselines. This trend supports the central premise of the work: in snapshot full-Stokes imaging, the quality of the encoded measurement is as critical as the power of the reconstruction algorithm.

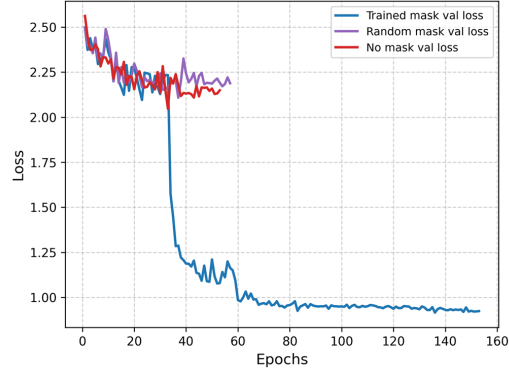


Figure 12: Loss function under different masks over training epochs in the RGB-achromatic case for the second stage.

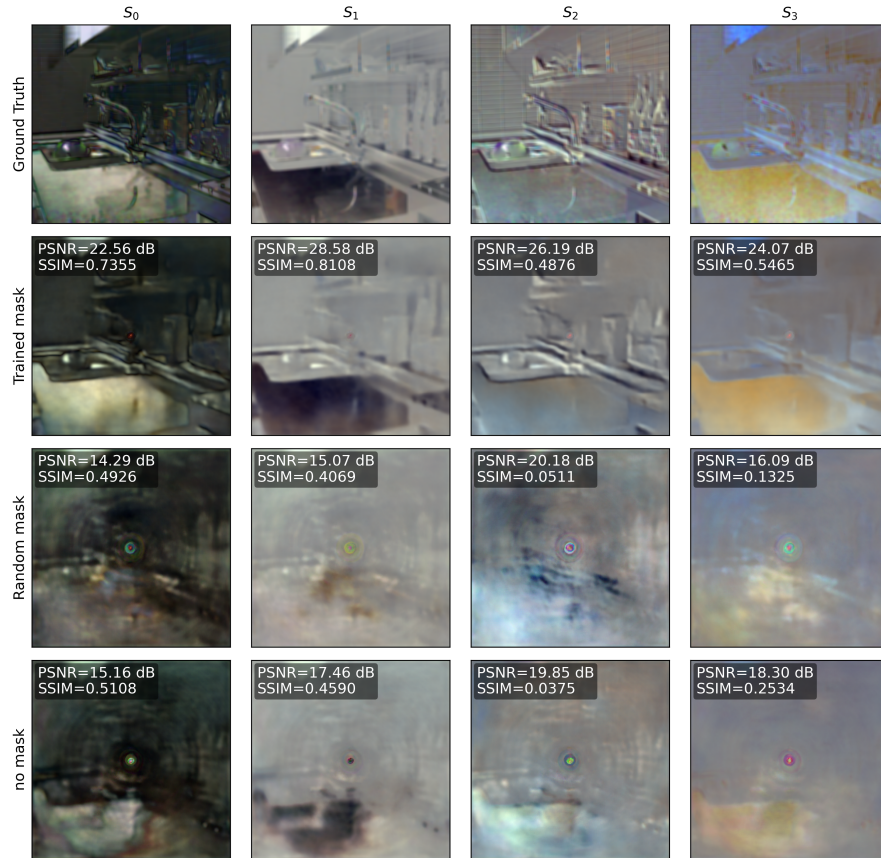


Figure 13: Examples of full-Stokes images reconstructed under different masks in the RGB-achromatic case for the second stage.

4 Summary and outlook

In summary, we have presented an end-to-end framework for snapshot full-Stokes polarization imaging that jointly optimizes a meta-optic frontend and a neural reconstruction backend. By embedding a trainable metasurface at the Fourier plane in a differentiable 4f system and using an MLP-based surrogate model of the polarization-dependent meta-atom response, the method learns an optical measurement operator tailored for full-Stokes recovery rather than prescribed optics-only target. This strategy is effective both in a hybrid metasurface-refractive system and in a pure meta-optic system obtained by replacing the refractive lenses with metalenses. On a real-world dataset, the framework

Table 6: Parameters and Performance of the State-of-the-Art Full-Stokes Reconstruction Works.

Wavelength (nm)	Snapshot capability	Compressive ratio	Dataset	Meta-optic architecture	MSE	PSNR	SSIM	ref
808	1	0.064	Synthetic	Pure	/	41.72	/	[4]
530	1	4	Synthetic	Hybrid	/	28.09	/	[44]
532	1	4	Synthetic	Hybrid	3.61×10^{-4}	39.46	0.9430	[21]
470	1	16	Synthetic	Pure	6.08×10^{-4}	/	/	[22]
520:10:690	1	1.53	Real-world	Hybrid	/	29.31~29.85	0.9~0.92	[45]
400:10:700	4	10.33	Real-world	Hybrid	/	34.83	0.9520	[13]
435.8	1	4	Real-world	Pure	4.34×10^{-4}	30.00	0.8291	Ours (lens)
435.8, 546.1, 700	1	12	Real-world	Pure	8.24×10^{-4}	26.71	0.7044	Ours (lens)
435.8	1	4	Real-world	Pure	7.58×10^{-4}	26.94	0.7184	Ours (metalens)
435.8, 546.1, 700	1	12	Real-world	Pure	1.55×10^{-3}	24.10	0.6015	Ours (metalens)

reconstructs monochromatic and RGB-achromatic full-Stokes images from a snapshot monochrome measurement, with the RGB configuration operating at a high compression ratio of 12.

Beyond the absolute reconstruction matrices, the central result is that co-designed optical encoding substantially improves the reconstructability of the inverse problem relative to fixed or unstructured encoders. This is especially important for full-Stokes imaging, where spectral and polarization information must be multiplexed into a single sensor plane under realistic physical constraints. Our results therefore depict a broader view of meta-optics not as standalone substitutes for conventional lenses, but as task-specific physical frontends whose potential can be fully unleashed when being optimized together with the reconstruction backends.

Looking forward, the remaining gap between the hybrid and pure meta-optic configurations shows that compactness still trades against optical quality when refractive elements are replaced by metalenses. Future work should therefore focus on more fabrication-robust designs, sensor-aware designs compatible with practical pixel sizes, and more expressive optical architectures such as single-piece, multilayer or nonlocal meta-optics [46–48]. Extending the present framework from three design wavelengths to continuous spectral bands and from static scenes to dynamic polarimetric imaging would further empower the applications in compact machine vision, remote sensing, and scientific imaging [49, 50].

References

- [1] G. Egan Walter. Polarization and surface roughness. In *PROCEEDINGS OF SPIE*, volume 3426, pages 144–152, 1998.
- [2] Edith Hartmann, Michel Lequime, Matthieu Castelnau, H el ene Krol, and Myriam Zerrad. All-dielectric metasurface polarization scrambler for imaging applications. *Physics Review A*, 112:043531, Oct 2025.
- [3] B. Chenault David and J. Larry Pezzaniti. Polarization imaging through scattering media. In *PROCEEDINGS OF SPIE*, volume 4133, pages 124–133, 2000.
- [4] Xiansong Ren, Ye Tian, Yanling Ren, Bo Wang, Shifeng Zhang, Anqi Hu, Kaveri A. Thakoor, and Xia Guo. Single-shot full-stokes imaging through scattering media. *Optica*, 12(10):1560–1568, 2025.
- [5] Zhineng Xie, Weihao Lin, Mengjiao Zhu, Jianmin Yang, Chenfan Shen, Xin Jin, Xiafei Qian, and Min Xu. Reciprocal polarization imaging of complex media. *Advanced Photonics Nexus*, 4(3):036010, 2025.
- [6] Jing Wang, Changzhong Jiang, Wenqing Li, and Xiangheng Xiao. Anisotropic low-dimensional materials for polarization-sensitive photodetectors: From materials to devices. *Advanced Optical Materials*, 10(6):2102436, 2022.
- [7] Seungri Song, Jeongsoo Kim, Taegyun Moon, Baekcheon Seong, Woovin Kim, Chang-Hyuk Yoo, Jun-Kyu Choi, and Chulmin Joo. Polarization-sensitive intensity diffraction tomography. *Light: Science & Applications*, 12(1):124, 2023.
- [8] Shuang Zhou, Jie Bian, Peng Chen, Mo Xie, Jie Chao, Wei Hu, Yanqing Lu, and Weihua Zhang. Polarization-dispersive imaging spectrometer for scattering circular dichroism spectroscopy of single chiral nanostructures. *Light: Science & Applications*, 11(1):64, 2022.
- [9] Frank Neubrech, Mario Hentschel, and Na Liu. Reconfigurable plasmonic chirality: Fundamentals and applications. *Advanced Materials*, 32(41):1905640, 2020.

- [10] Shuaibao Chen, Peng Liu, Wei He, Dong Luo, Yuguang Tan, Liangpei Chen, Jue Wang, Qi Zhao, Guohua Jiao, and Wei Chen. Polarization-enhanced underwater laser range-gated imaging for subaquatic applications. *Sensors*, 24(20):6681, 2024.
- [11] Lawrence B. Wolff. Polarization vision: a new sensory approach to image understanding. *Image Vision Computing*, 15(2):81–93, 1997.
- [12] Yu Lei, Bing Lei, Yubo Cai, Chao Gao, and Fujie Wang. Polarimetric dehazing method based on image fusion and adaptive adjustment algorithm. *Applied Sciences*, 11(21):10040, 2021.
- [13] Jingyue Ma, Zhenming Yu, Zhengyang Li, Liang Lin, Liming Cheng, Jiayu Di, Tongshuo Zhang, Ning Zhan, and Kun Xu. Integrated diffractive full-stokes spectro-polarimetric imaging. *Optics Express*, 33(24):51223–51236, 2025.
- [14] Davide Pierangeli, Giovanni Volpe, and Claudio Conti. Deep learning enabled transmission of full-stokes polarization images through complex media. *Laser & Photonics Reviews*, 18(11):2400626, 2024.
- [15] Davide Pierangeli and Claudio Conti. Single-shot polarimetry of vector beams by supervised learning. *Nature Communications*, 14(1):1831, 2023.
- [16] Mohammadreza Khorasaninejad, Wei Ting Chen, Robert C. Devlin, Jaewon Oh, Alexander Y. Zhu, and Federico Capasso. Metalenses at visible wavelengths: Diffraction-limited focusing and subwavelength resolution imaging. *Science*, 352(6290):1190–1194, 2016.
- [17] Wei Ting Chen, Joon-Suh Park, Justin Marchioni, Sophia Millay, Kerolos M. A. Yousef, and Federico Capasso. Broadband, high-efficiency metasurfaces using dispersion-engineered nanostructures. In *Conference on Lasers and Electro-Optics(CLEO) 2024*, page FM3L.7. Optica Publishing Group, 2024.
- [18] Zhou Jun-zhuo, H. A. O. Jia, Y. U. Xiao-chang, Zhou Jian, Deng Chen-wei, and Y. U. Yi-ting. Recent advances in metasurfaces for polarization imaging. *Chinese Optics*, 16(5):973–995, 2023.
- [19] J. P Balthasar Mueller, Noah A. Rubin, Robert C. Devlin, Benedikt Groever, and Federico Capasso. Metasurface polarization optics: Independent phase control of arbitrary orthogonal states of polarization. *Physical Review Letters*, 118(11):113901, 2017.
- [20] Seung-Hwan Baek, Hayato Ikoma, Daniel S Jeon, Yuqi Li, Wolfgang Heidrich, Gordon Wetzstein, and Min H Kim. Single-shot hyperspectral-depth imaging with learned diffractive optics. In *Proceedings of the IEEE/CVF International Conference on Computer Vision*, pages 2651–2660, 2021.
- [21] Huai Xia, Bingliang Chen, Changwei Zhang, Xi Zhu, Chang Wang, and Zhenrong Zheng. Joint optimization of coded aperture metasurface and residual self-attention network for snapshot full-stokes imaging. *Optics Express*, 32(17):29609–29619, 2024.
- [22] Gaurav Arya, William F. Li, Charles Roques-Carmes, Marin Soljačić, Steven G. Johnson, and Zin Lin. End-to-end optimization of metasurfaces for imaging with compressed sensing. *ACS Photonics*, 11(5):2077–2087, 2024.
- [23] Zin Lin, Raphaël Pestourie, Charles Roques-Carmes, Zhaoyi Li, Federico Capasso, Marin Soljačić, and Steven G. Johnson. End-to-end metasurface inverse design for single-shot multi-channel imaging. *Optics Express*, 30(16):28358–28370, 2022.
- [24] Zin Lin, Charles Roques-Carmes, Raphaël Pestourie, Marin Soljačić, Arka Majumdar, and Steven G. Johnson. End-to-end nanophotonic inverse design for imaging and polarimetry. *Nanophotonics*, 10(3):1177–1187, 2021.
- [25] Sophie Fisher, Gaurav Arya, Arka Majumdar, Zin Lin, and Steven G. Johnson. End-to-end metasurface design for temperature imaging via broadband planck-radiation regression. *Advanced Optical Materials*, 13(9):2402498, 2025.
- [26] Yu-Cheng Chu, Tzu-Yu Peng, Chen-Yu Wang, Shyr-Shyan Yeh, Jia-Wern Chen, and Yu-Jung Lu. Polarization-encoded color images for information encryption enabled by hfn refractory plasmonic metasurfaces. *Nanophotonics*, 14(25):4655–4664, 2025.
- [27] Y. Jeon, E. Choi, Y. Kim, Y. Moon, K. Omer, F. Heide, and S. H. Baek. Spectral and polarization vision: Spectro-polarimetric real-world dataset. In *2024 IEEE/CVF Conference on Computer Vision and Pattern Recognition (CVPR)*, pages 22098–22108, 2024.
- [28] Zhaoyi Li, Raphaël Pestourie, Joon-Suh Park, Yao-Wei Huang, Steven Johnson, and Federico Capasso. Inverse design enables large-scale high-performance meta-optics reshaping virtual reality. *Nature Communications*, 13(1):2409, 2022.
- [29] Raphaël Pestourie, Wenjie Yao, Boubacar Kanté, and Steven G. Johnson. Efficient inverse design of large-area metasurfaces for incoherent light. *ACS Photonics*, 10(4):854–860, 2023.

- [30] Luca Sacchi, Alfonso Palmieri, Vitthal Mishra, Joon-Suh Park, Marco Piccardo, and Federico Capasso. Silica meta-optics: When high performance does not need a high index. *Nano Letters*, 25(50):17448–17457, 2025.
- [31] Noah A. Rubin, Aun Zaidi, Ahmed H. Dorrah, Zhujun Shi, and Federico Capasso. Jones matrix holography with metasurfaces. *Science Advances*, 7(33):eabg7488, 2021.
- [32] Ardavan F. Oskooi, David Roundy, Mihai Ibanescu, Peter Bermel, J. D. Joannopoulos, and Steven G. Johnson. Meep: A flexible free-software package for electromagnetic simulations by the fdtd method. *Computer Physics Communications*, 181(3):687–702, 2010.
- [33] Raphaël Pestourie, Carlos Pérez-Arancibia, Zin Lin, Wonseok Shin, Federico Capasso, and Steven G. Johnson. Inverse design of large-area metasurfaces. *Optics Express*, 26(26):33732–33747, 2018.
- [34] Zin Lin, Victor Liu, Raphael Pestourie, and Steven G. Johnson. Topology optimization of freeform large-area metasurfaces. *Optics Express*, 27(11):15765–15775, 2019.
- [35] Raphaël Pestourie, Carlos Pérez-Arancibia, Zin Lin, Wonseok Shin, Federico Capasso, and Steven G. Johnson. Inverse design of large-area metasurfaces. *Optics Express*, 26(26):33732–33747, 2018.
- [36] Haejun Chung, Feng Zhang, Hao Li, Owen D. Miller, and Henry I. Smith. Inverse design of high-na metalens for maskless lithography. *Nanophotonics*, 12(13):2371–2381, 2023.
- [37] Elyas Bayati, Raphaël Pestourie, Shane Colburn, Zin Lin, Steven G. Johnson, and Arka Majumdar. Inverse designed metalenses with extended depth of focus. *ACS Photonics*, 7(4):873–878, 2020.
- [38] Wei Ting Chen, Alexander Y. Zhu, Vyshakh Sanjeev, Mohammadreza Khorasaninejad, Zhujun Shi, Eric Lee, and Federico Capasso. A broadband achromatic metalens for focusing and imaging in the visible. *Nature Nanotechnology*, 13(3):220–226, 2018.
- [39] Zhaoyi Li, Peng Lin, Yao-Wei Huang, Joon-Suh Park, Wei Ting Chen, Zhujun Shi, Cheng-Wei Qiu, Ji-Xin Cheng, and Federico Capasso. Meta-optics achieves rgb-achromatic focusing for virtual reality. *Science Advances*, 7(5):eabe4458, 2021.
- [40] M. Khorasaninejad, A. Y. Zhu, C. Roques-Carmes, W. T. Chen, J. Oh, I. Mishra, R. C. Devlin, and F. Capasso. Polarization-insensitive metalenses at visible wavelengths. *Nano Letters*, 16(11):7229–7234, 2016.
- [41] Mengdi Sun, Ata Shakeri, Arvin Keshvari, Dimitrios Giannakopoulos, Qing Wang, Wei-Ting Chen, Steven G. Johnson, and Zin Lin. Scalable freeform optimization of wide-aperture 3d metalenses by zoned discrete axisymmetry. *ACS Photonics*, 12(6):3163–3171, 2025.
- [42] Amir Arbabi, Yu Horie, Mahmood Bagheri, and Andrei Faraon. Dielectric metasurfaces for complete control of phase and polarization with subwavelength spatial resolution and high transmission. *Nature Nanotechnology*, 10(11):937–943, 2015.
- [43] William F. Li, Gaurav Arya, Charles Roques-Carmes, Zin Lin, Steven G. Johnson, and Marin Soljačić. Transcending shift-invariance in the paraxial regime via end-to-end inverse design of freeform nanophotonics. *Optics Express*, 31(15):24260–24272, 2023.
- [44] Huai Xia, Qiangbo Zhang, Changwei Zhang, Mengguang Wang, Yiyang Liu, Chang Wang, and Zhenrong Zheng. Inverse design of cascaded multidimensional coding metasurface for snapshot full-stokes imaging and depth estimation. *ACS Photonics*, 12(11):6502–6510, 2025.
- [45] Axin Fan, Tingfa Xu, Geer Teng, Xi Wang, Chang Xu, Yuhan Zhang, Xin Xu, and Jianan Li. Deep learning reconstruction enables full-stokes single compression in polarized hyperspectral imaging. *Chinese Optics Letters*, 21(5):051101, 2023.
- [46] L. Stefanini, D. Ramaccia, M. Barbuto, Z. Hamzavi-Zarghani, M. Longhi, A. Monti, S. Vellucci, A. Toscano, and F. Bilotti. A statistical approach for robust metasurfaces and metasurface-based ris engineering. *IEEE Transactions on Antennas and Propagation*, 72(6):5402–5407, 2024.
- [47] You Zhou, Ivan I Kravchenko, Hao Wang, J Ryan Nolen, Gong Gu, and Jason Valentine. Multilayer noninteracting dielectric metasurfaces for multiwavelength metaoptics. *Nano letters*, 18(12):7529–7537, 2018.
- [48] Guoce Yang, Mengyun Wang, June Sang Lee, Nikolaos Farmakidis, Joe Shields, Carlota Ruiz de Galarreta, Stuart Kendall, Jacopo Bertolotti, Andriy Moskalenko, Kairan Huang, et al. Nonlocal phase-change metaoptics for reconfigurable nonvolatile image processing. *Light: Science & Applications*, 14(1):182, 2025.
- [49] Shane Colburn, Alan Zhan, and Arka Majumdar. Metasurface optics for full-color computational imaging. *Science Advances*, 4(2):eaar2114, 2018.

- [50] Luocheng Huang, Zheyi Han, Anna Wirth-Singh, Vishwanath Saragadam, Saswata Mukherjee, Johannes E. Fröch, Quentin A. A. Tanguy, Joshua Rollag, Ricky Gibson, Joshua R. Hendrickson, Philip W. C. Hon, Orrin Kigner, Zachary Coppens, Karl F. Böhringer, Ashok Veeraraghavan, and Arka Majumdar. Broadband thermal imaging using meta-optics. *Nature Communications*, 15(1):1662, 2024.